PHYSICAL REVIEW B VOLUME 43, NUMBER 12 15 APRIL 1991-II

# Electronic and magnetic structure of {111} stacking faults in nickel

D. C. Chrzan
*Sandia National Laboratories, Livermore, California 94551*

L. M. Falicov
*Materials Sciences Division, Lawrence Berkeley Laboratory, Berkeley, California 94720*
*and Department of Physics, University of California, Berkeley, California 94720*

J. M. MacLaren
*Department of Physics, Tulane University, New Orleans, Louisiana 70118*

X.-G. Zhang
*Center for Advanced Materials, Materials and Chemical Sciences Division, Lawrence Berkeley Laboratory,*
*Berkeley, California 94720*

A. Gonis
*Chemistry and Materials Science, L-280, Lawrence Livermore National Laboratory, Livermore, California 94550*

(Received 16 July 1990)

The electronic and magnetic structure of {111} stacking faults in nickel is investigated utilizing a fully self-consistent, layered multiple-scattering approach which does not require full three-dimensional symmetry or the use of finite-size slabs. The electronic and magnetic structures of a twin boundary, an intrinsic fault, an extrinsic fault, and two other stacking sequences are calculated. In addition, total energies of the faults are calculated and found to be in good agreement with the available experimental results. Localized states appear in all the studied stacking faults; the state's energies and exchange splittings are tabulated. The presence of a stacking fault results in a decrease in the spin polarization near the faults. This decrease arises from subtle changes in the electronic structure arising from the fault. For all the faults, the spin polarization is found to be insensitive to the orientation of the nearest-neighbor atoms, but instead can be related to the distance to the nearest atom in the direction perpendicular to the fault plane. Very simple empirical expressions for calculating the total energy and spin polarization of *any* stacking configuration are presented.

## I. INTRODUCTION

Stacking faults are known to influence elastic properties of metals and may also influence bulk magnetic properties through magnetic-domain-wall–stacking-fault interactions. It follows that the electronic and magnetic structure of {111} stacking faults in transition metals is of considerable interest. Recently, attention has been focused on the theoretical[1-6] and experimental properties[7-14] of transition-metal films and surfaces, but relatively little attention has been given to planar defects in bulk transition metals. This is somewhat surprising since a thorough understanding of {111} stacking faults in the pure transition metals may lead to a better understanding of transition-metal films and surfaces.

This paper is concerned with the calculation of the electronic and magnetic properties of {111} stacking faults in nickel. Yndurain and Falicov[15] studied this problem using an unpolarized tight-binding method and found that localized electronic states appear at the interfaces, but they did not examine the faults' magnetic structure. Grise *et al.*[16] performed tight-binding calculations utilizing large unit cells containing stacking faults and found a 3% change in the spin polarization on the central layer of an extrinsic fault as well as a rich electronic structure including numerous localized states, but they did not calculate total energies for the faults.

Recent advances in electronic-structure calculations permit a fully self-consistent calculation of the faults' properties without the imposition of periodic boundary conditions or the use of finite-size slabs. The electronic and magnetic structures are calculated exactly, within the one-electron local-spin-density approximation, using a fully self-consistent layer–Korringa-Kohn-Rostoker (LKKR) technique.[17]

The spin polarization and total energies of face-centered-cubic (fcc) nickel, hexagonal-close-packed (hcp) nickel, and several types of stacking faults are calculated and analyzed. The calculated total energies agree well with experimental estimates. It is argued that small changes in the spin polarization at a stacking defect are the result of two, subtle effects: (1) a symmetry-induced rearrangement of the majority-spin states near the Fermi level and (2) a local broadening in the bandwidth of the minority-spin band which crosses the Fermi level. The energies and exchange splittings of the localized states, which appear at all of the studied faults, are calculated and tabulated. In addition, the total energies and spin polarization are fitted to simple empirical expressions which can be used to calculate the properties of any stacking sequence.

Section II of this paper contains a brief description of the method of calculation. Section III presents the results of the calculations. Section IV contains the analysis of the results, and simple empirical relations for the spin polarization and total energy are discussed and analyzed in Sec. V. The conclusions are presented in Sec. VI.

## II. METHOD OF CALCULATION

In the LKKR method, the properties of a three-dimensional periodic solid are calculated by dividing the solid into two-dimensional planar components. The method proceeds by first calculating the $T$ matrix of a two-plane unit. The $T$ matrix of the two-plane unit is then used to generate the $T$ matrix of the four-plane unit. This process, referred to as layer doubling,[18] is repeated until the $T$ matrix of a complete half-space is generated. The $T$ matrices for the left and right half-spaces are then combined to generate the $T$ matrix of the complete solid. Layer doubling provides an extremely efficient method for calculating the properties of the three-dimensional solid.

Once the $T$ matrix of the entire solid is known, the single-particle Green's function is calculated from the Dyson equation,

$$G = G_0 + G_0 T G_0 \ , \tag{1}$$

where $G_0$ is the free-particle Green's function and $T$ is the $T$ matrix for the complete solid. The Green's function can then be used to calculate the physical properties of the solid. For example, the spectral function [spatial- and energy-resolved density of states (DOS)], $\rho(\mathbf{r},E)$, is given by

$$\rho(\mathbf{r},E) = -(1/\pi)\,\mathrm{Im}G(\mathbf{r},\mathbf{r},E) \ , \tag{2}$$

where $\mathbf{r}$ denotes the position and $E$ denotes the energy. The spectral function can then be used to calculate the charge density, Fermi energy, and electronic energy of the system merely by integrating over the appropriate variable with the appropriate weighting factor.

In the self-consistent iterations, the charge density calculated from the Green's function is used to generate a new potential which includes contributions from both the Coulomb interaction with the nuclei and other electrons, and the exchange-correlation potential in the local-spin-density approximation (by means of the expression of Hedin and Lundqvist[19]). The generated potential is then converted to the so-called muffin-tin form, an approximation which is known to produce good results for close-packed metals. The phase shifts of these potentials are calculated, including the semirelativistic corrections of Koelling and Harmon,[20] and a new $T$ matrix is calculated. (Spin-orbit coupling, which is probably only important in the regions of $\mathbf{k}$ space where two bands of opposite polarization cross near the Fermi level, is neglected.) The entire process is then iterated to self-consistency.

The LKKR formalism easily adapts to a three-dimensional system containing a stacking defect. In calculating the properties of a stacking defect, the first step is to characterize completely the bulk material. The second step embeds $N$ layers of material, containing the stacking defect, within the bulk system. The self-consistent formalism described above is then applied to the $N$-layer region; the potentials of the atoms in the $N$ layers are allowed to change but the potentials in the bulk regions are restricted to having their bulk values, as is the Fermi level of the complete system (stacking fault and bulk). The constraint that the potentials be bulklike outside the $N$-layer region provides the boundary condition for the adjusted region. Structural relaxations near the faults are not considered. The close-packed structure of the stacking faults suggests that this is a good approximation.

A mixed basis set is used in the LKKR method. The multiple-scattering equations in each plane are solved in a spherical-wave basis containing the $l=0$ to $l=2$ ($s$, $p$, and $d$) partial waves. The spherical-wave basis is then transformed into a plane-wave basis containing 19 plane waves. The plane-wave basis is used to connect the separate planes. A triangular contour, containing 28 points in the upper-half complex energy plane, is used for the energy integrations. It is necessary to use 45 $\mathbf{k}$ points in an irreducible wedge of the two-dimensional Brillouin zone to obtain convergence. Earlier calculations[21] using only six $\mathbf{k}$ points and eight points for the energy contour produced results with similar trends in spin polarization although larger in magnitude and similar total energies. For the bulk systems, the potentials are iterated until the Fermi energies are stable to at least $10^{-5}$ hartree. The potentials of the interface calculations were iterated to obtain a similar accuracy. At this level of self-consistency, the spin polarizations are stable to better than $\pm 0.001\mu_B$, where $\mu_B$ is the Bohr magneton.

## III. RESULTS

The muffin-tin density of states (MTDOS), i.e., the density of states resulting from integrating $\rho(\mathbf{r},E)$ over the muffin tin, for fcc nickel is shown in Fig. 1. The nearest-neighbor distance was chosen to be that of Moruzzi, Janak, and Williams[22]—4.631 55 a.u. The calculated Fermi energy is 0.3530 hartree above the muffin-tin zero (all energies are quoted relative to the muffin-tin zero), and the muffin-tin spin polarization, which is the polarization of the charge within the muffin-tin radius, is $0.584\mu_B$. The spin polarization of the charge within the Wigner-Seitz sphere is $0.569\mu_B$, indicating that the interstitial charge is polarized in the directions opposite to that in the muffin tin, a feature common to all the calculations below. The exchange splitting, as measured by the peak in the MTDOS closest to the Fermi level is 0.022 hartree (0.60 eV), which agrees well with the value 0.68 eV given[23] by Wang and Callaway.

The electronic and magnetic properties of hcp nickel, with ideal $c/a$ ratio, were also calculated. The nearest-neighbor distance was fixed to be the bulk fcc value quot-

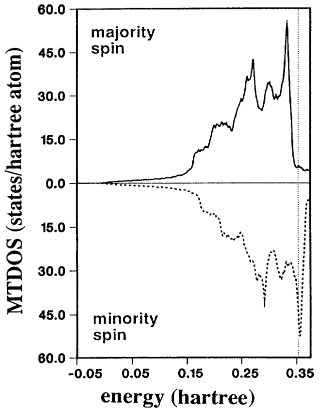

FIG. 1. The muffin-tin density of states (MTDOS) for bulk fcc nickel. The solid line is the majority spin and the dashed line is the minority spin. The dotted line represents the Fermi level.

ed above. While the hcp phase of nickel is not seen experimentally, its calculated properties can be used to help in understanding the properties of $\{111\}$ stacking faults in the fcc phase. ($\{111\}$ stacking faults have layers of atoms in which the nearest-neighbor atoms occupy the positions they would occupy in the hcp lattice.) The Fermi level of hcp nickel is found to lie at 0.3534 hartree. The spin polarization within the muffin tin is $0.579\mu_B$; that within the Wigner-Seitz sphere is $0.564\mu_B$. The spin polarization changes by less than 1% in going from the fcc phase to the hcp phase; one expects that the changes in spin polarization near a stacking fault should be similar in magnitude. The calculated total energy of the hcp phase is 85 erg/cm$^2$ (111)-plane larger than the total energy of the fcc phase.

The $ABC$ notation[24] is used to describe the stacking of the (111) planes. Each (111) plane forms a triangular net. There are two distinct (low-energy) sites in layer $A$ on which the next (111) plane can be stacked, referred to as $B$ and $C$. The fcc structure is built by stacking the planes in the sequence $ABCABC$, and the hcp structure is constructed by stacking the planes in the sequence $ABABAB$. In the notation used below, the fcc structure is denoted by $(\cdots\langle ABC\rangle\cdots)$ where the angular brackets indicate that the structure within them is repeated to infinity in the direction indicated by the bracket immediately adjacent to the "$\cdots$." Hence the hcp structure is denoted by $(\cdots\langle AB\rangle\cdots)$. The five types of faults investigated are shown in Fig. 2 and are referred to as (a) a twin-boundary fault $(\cdots\langle BCA\rangle B\langle ABC\rangle\cdots)$, (b) an intrinsic fault $(\cdots\langle CAB\rangle\langle ABC\rangle\cdots)$, (c) an extrinsic fault $(\cdots\langle CAB\rangle A\langle CAB\rangle\cdots)$, and, for the lack of established names, (d) a superextrinsic fault $(\cdots\langle BCA\rangle CB\langle ABC\rangle\cdots)$ and (e) a hyperextrinsic fault $(\cdots\langle BCA\rangle CBA\langle CAB\rangle\cdots)$. (The letters in Fig. 2 are staggered to aid in visualizing the structure of the faults.) The number of layers allowed to readjust in each calculation is the number of pictured layers less 2 (the two end layers were constrained to be bulklike). Each of the faults (b)–(e) is composed of twin-boundary faults separated by 0–3 (111) planes, respectively. An analysis of the trends in this series of faults should provide a good indication of the importance of interactions between twin-boundary faults, as well as healing lengths for the electronic and magnetic structure.

The muffin-tin spin polarizations for each of the stacking sequences are presented in Table I. (Muffin-tin spin polarizations are quoted because full-cell spin polarizations are unavailable. The Wigner-Seitz approximation to the full-cell polarizations shows trends identical to those demonstrated in the muffin-tin spin polarizations.) The labeling of the layers in Table I corresponds to that shown in Fig. 2, where the first entry under each structure is the uppermost layer in Fig. 2. Since the spin polarizations are symmetric about the midpoints of the faults (indicated by arrows in Table I), the table contains

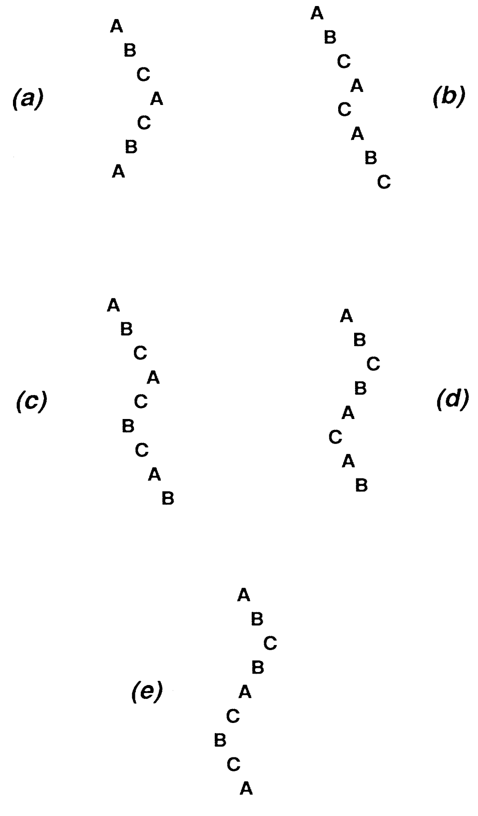

FIG. 2. The investigated stacking faults: (a) The twin-boundary fault, (b) the intrinsic fault, (c) the extrinsic fault, (d) the superextrinsic fault, and (e) the hyperextrinsic fault. The layers allowed, in the calculation, to adjust for the presence of the fault are those shown, with the exception, in each case, of the top and bottom layers, which are restricted to having the electronic and magnetic structure of the bulk. The letters are staggered to aid in visualization of the stacking-fault structure (the [111] direction of the lattice points straight up in the figure).

TABLE I. Muffin-tin spin polarization ($\mu_B$). The muffin-tin spin polarization of the bulk hcp structure is $0.579\mu_B$. The arrows indicate the central point of each fault.

| Twin | | Intrinsic | | Extrinsic | | Superextrinsic | | Hyperextrinsic | |
|---|---|---|---|---|---|---|---|---|---|
| *A* | 0.584 | *A* | 0.584 | *A* | 0.584 | *A* | 0.584 | *A* | 0.584 |
| *B* | 0.584 | *B* | 0.585 | *B* | 0.584 | *B* | 0.579 | *B* | 0.579 |
| *C* | 0.579 | *C* | 0.579 | *C* | 0.580 | *C* | 0.584 | *C* | 0.587 |
| →*A* | 0.587 | *A* | 0.582 | *A* | 0.586 | *B* | 0.577 | *B* | 0.579 |
| | | → | | →*C* | 0.571 | → | | →*A* | 0.583 |

the results for only the upper half of each fault. The values of the spin polarization for layers immediately adjacent to the bulk suggest that the regions in which the potential is allowed to readjust are sufficiently large. The changes in spin polarizations induced by the presence of a fault are very small, the largest difference (the central layer of the extrinsic fault) representing only a 2% decrease in spin polarization. This difference should be compared with the 16% reduction in spin polarization of the {111} surface predicted by tight-binding theory.[4,5]

Table II contains the calculated values for the stacking-fault energies. The energy of a single twin-boundary fault is 78±5 erg/cm$^2$. (The error bars reflect the numerical stability of the calculation.) The energies of the remaining faults are roughly twice that of the twin-boundary fault, which is consistent with the fact that each of the faults is composed of two twin-boundary faults. The energy of the extrinsic fault is slightly less than twice the twin-boundary fault, indicating that there is a slight interaction between two twin boundaries separated by one (111) plane.

Overall, the agreement between the theoretical result and experimental results is quite impressive. Experimental estimates[25] for the intrinsic stacking fault range from 79 to 410 erg/cm$^2$, with the best estimates near 120–130 erg/cm$^2$. The calculations presented here give the value of 155 erg/cm$^2$.

Figure 3(a) is the two-dimensional Brillouin zone used for the calculations. The dashed line demarcates the irreducible wedge over which the integrations were performed. Each point in the two-dimensional Brillouin zone corresponds to a direction in the three-dimensional Brillouin zone. For example, the $\bar{\Gamma}$ point includes all the states with **k** directed along the $\Gamma-L$ direction. This is indicated in Fig. 3(b) by labeling the $\bar{\Gamma}$ point by $\Gamma$ and $L$. Similarly, the $\bar{M}$ point includes all the states with **k** directed along the $L-X$ direction. (The two-dimensional projection points of the $K$ points of the three-dimensional zone are shown for completeness.) Any alteration in the spin polarization resulting from a stacking fault will involve the majority- and minority-spin states nearest to the Fermi level. The minority-spin states pass through the Fermi level along the $\Gamma-X$ and $\Gamma-L$ directions. Hence changes in these states should be reflected in the $\bar{M}$ and $\bar{\Gamma}$ MTDOS, respectively. The majority-spin states nearest the Fermi level lie along the $X-W$ directions. Changes in the states at $X$ should be reflected in the $\bar{M}$ MTDOS.

Figure 4 is the two-dimensional projection of the three-dimensional band structure of fcc nickel, plotted along the symmetry directions of the two-dimensional zone. The shaded regions of this figure correspond to points for which three-dimensional band states exist. The

TABLE II. Total energies of stacking faults.

| System | Energy (erg/cm$^2$) | Fitted energy (erg/cm$^2$) |
|---|---|---|
| Twin | 78±5 | 81 |
| Intrinsic | 155±5 | 150 |
| Extrinsic | 145±5 | 156 |
| Superextrinsic | 160±10 | 150 |
| Hyperextrinsic | 170±10 | 162 |

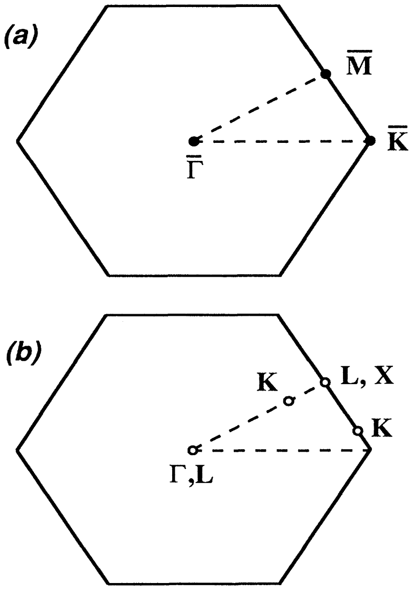

FIG. 3. Panel (a) is the two-dimensional Brillouin zone used in the calculations. The dashed line demarcates the irreducible wedge over which the integrations were performed. Panel (b) show the projection points of the symmetry points of the full three-dimensional Brillouin zone of the fcc lattice, labeled by their corresponding three-dimensional labels.

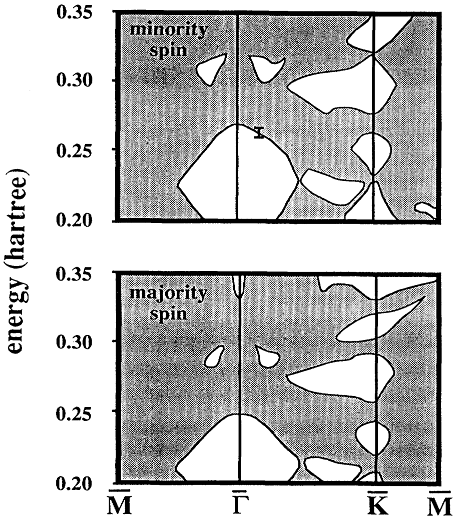

FIG. 4. The two-dimensional projected band structure of bulk fcc nickel. The shaded regions of this plot correspond to points for which three dimensionally extended band states exist. The white regions, in which no three-dimensional band states are found, are the regions where localized states may be found. The error bar indicates the accuracy to which the figure is drawn. From the figure it is clear that localized states (in the depicted energy range) may be found near $\overline{\Gamma}$ and $\overline{K}$, but not near $\overline{M}$.

white regions are gaps for which there are no three-dimensional band states. Localized states can appear in these gaps. Evidently, there is the possibility of finding localized states in the immediate vicinities of $\overline{\Gamma}$ and $\overline{K}$, but not about $\overline{M}$ (for this range of energies).

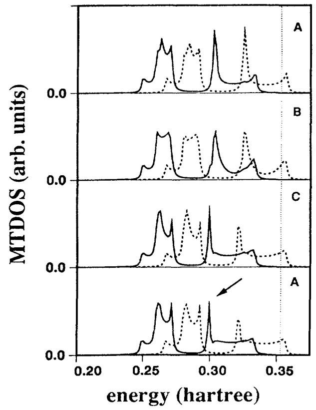

FIG. 5. The layer-projected MTDOS for the $\overline{\Gamma}$ point of the twin-boundary fault. The solid curve is the majority-spin states and the dashed curve is the minority-spin states. The dotted line represents the Fermi energy. The labels correspond to the layers contained in Table I. The arrow indicates the majority-spin resonant states. (The corresponding minority-spin resonant state, *not* indicated by an arrow, lies 0.021 hartree above the majority-spin state.) (The energies and exchange splittings of the resonance are given in Table III.)

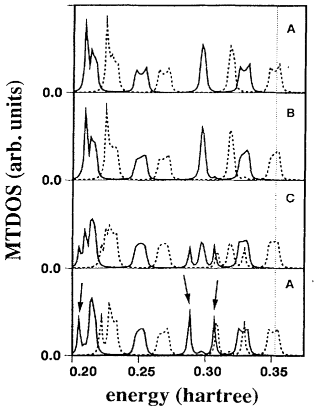

FIG. 6. The layer-projected MTDOS for the $\overline{K}$ point of the twin-boundary fault. The solid curve is the majority-spin states and the dashed curve is the minority-spin states. The dotted line represents the Fermi energy. The labels correspond to the layers contained in Table I. The arrows indicate the majority-spin localized states. (The corresponding minority-spin localized states, *not* indicated by arrows, lie approximately 0.02 hartree above their majority-spin counterparts.) (The energies and exchange splittings of the states are given in Table III).

Layer-projected MTDOS were calculated and plotted for the $\overline{\Gamma}$ and $\overline{K}$ points in the two-dimensional Brillouin zone for all of the studied faults. In all cases, states localized at $\overline{K}$ were found. In addition, a nearly localized resonance was found at $\overline{\Gamma}$. The energies and exchange splittings of the localized states are tabulated in Table III. These states may be observable in photoemission experiments, although their presence may be masked by surface states. Figures 5 and 6 are the layer-projected MTDOS for $\overline{\Gamma}$ and $\overline{K}$ of the twin boundary, respectively. The $\overline{\Gamma}$ resonance (Fig. 5) is clearly visible at 0.300 hartree (0.321 hartree) in the majority (minority) spin. In addition, the three localized states at $\overline{K}$ are also apparent (Fig. 6).

## IV. ANALYSIS

This section of the paper is divided into two separate subsections. The first considers the effects of the stacking faults on the spin polarization near the faults. The second analyzes the properties of the localized states.

### A. Magnetic structure

As stated above, the changes in spin polarization induced by the presence of the faults represent a very small percentage change, the largest change (the central layer of the extrinsic fault) corresponding to approximately 2%. While the effects reported here are most likely to be too small to be observed experimentally, an understanding of the source of the changes in spin polarization may be useful in predicting the magnetic properties of stacking faults in other materials, e.g., cobalt.

The Wigner-Seitz-sphere spin polarization on the central layer of the extrinsic fault is $0.556\mu_B$, which is re-

TABLE III. Energies and exchange splittings of localized states (energies are in hartrees). Asterisks indicate that the state appeared as a shoulder on another peak.

| | $\bar{\Gamma}$ | | | $\bar{K}$ | | |
|---|---|---|---|---|---|---|
| Structure | Majority | Minority | Splitting | Majority | Minority | Splitting |
| Twin | 0.300 | 0.321 | 0.021 | 0.307 | 0.330 | 0.023 |
| | | | | 0.289 | 0.308 | 0.019 |
| | | | | 0.205 | 0.221 | 0.016 |
| Intrinsic | 0.297 | 0.320 | 0.023 | 0.313 | 0.335 | 0.022 |
| | | | | 0.294 | 0.316 | 0.022 |
| | | | | 0.286 | 0.307 | 0.021 |
| | | | | 0.204 | 0.219 | 0.015 |
| Extrinsic | 0.299 | 0.320 | 0.021 | 0.307 | 0.330 | 0.023 |
| | | | | 0.289 | 0.308 | 0.019 |
| | | | | 0.205 | 0.222 | 0.017 |
| Superextrinsic | 0.300 | 0.321 | 0.021 | 0.307 | 0.330 | 0.023 |
| | | | | 0.289 | 0.308 | 0.019 |
| | | | | 0.205 | 0.222 | 0.017 |
| Hyperextrinsic | 0.300 | 0.322 | 0.021 | 0.308 | * | * |
| | | | | 0.306 | 0.328 | 0.022 |
| | | | | 0.289 | 0.308 | 0.019 |
| | | | | 0.205 | 0.222 | 0.017 |

duced from the bulk fcc value, $0.569\mu_B$. An analysis of the angular-momentum-resolved charge distribution aids in understanding the source of this reduction. Table IV contains the angular-momentum-resolved Wigner-Seitz-sphere charges (excluding the core electrons) for bulk fcc nickel, bulk hcp nickel, and the central layer of the extrinsic fault. This table also contains the angular-momentum-resolved difference in charge between the bulk fcc structure and the two other structures.

Analysis of the data in the table indicates that the change in spin polarization in going from the fcc to the hcp structure arises, in the calculation, via a transfer of charge from the majority-spin *s*, *d*, and mostly *p* states into the minority-spin *d* states. This is exactly what one would expect from the structure of the density of states in bulk fcc nickel where the majority-spin states nearest to the Fermi level are *s* and *p* states, and the Fermi level passes through the minority-spin *d* states. These minority-spin *d* states have wave vectors lying along the $\Gamma$ to $L$ line ([111] direction) of the full three-dimensional Brillouin zone, and hence are likely to be influenced by the changes in symmetry of the crystal along that direction.

Details of the change in electronic structure leading to the reduction in the spin polarization are reflected in Figs. 7 and 8. Figure 7 compares the MTDOS of hcp and fcc nickel at $\bar{\Gamma}$. The $\bar{\Gamma}$ point includes those states with **k** along the $\Gamma$ to $L$ direction of the fcc three-dimensional Brillouin zone; the corresponding states in the hcp zone lie along $\Gamma$ to $A$. The *d* band nearest to the Fermi level is significantly broadened in the hcp case. In addition, the minority peak nearest to the Fermi level lies, in the hcp structure, completely below the Fermi level. The band broadening is consistent with the fact that the effective

TABLE IV. Wigner-Seitz charge distribution.

| | | Majority spin | | Minority spin | | Total charge | |
|---|---|---|---|---|---|---|---|
| | | Charge | Difference | Charge | Difference | Charge | Difference |
| fcc | *s* | 0.3256 | | 0.3291 | | 0.6547 | |
| | *p* | 0.3663 | | 0.3858 | | 0.7521 | |
| | *d* | 4.5928 | | 4.0004 | | 8.5932 | |
| hcp | *s* | 0.3253 | −0.0003 | 0.3279 | −0.0012 | 0.6532 | −0.0015 |
| | *p* | 0.3647 | −0.0016 | 0.3855 | −0.0003 | 0.7502 | −0.0019 |
| | *d* | 4.5922 | −0.0006 | 4.0044 | 0.0040 | 8.5966 | 0.0034 |
| ext. | *s* | 0.3252 | −0.0004 | 0.3285 | −0.0006 | 0.6537 | −0.0010 |
| | *p* | 0.3640 | −0.0023 | 0.3849 | −0.0009 | 0.7489 | −0.0032 |
| | *d* | 4.5884 | −0.0044 | 4.0079 | 0.0075 | 8.5963 | 0.0031 |

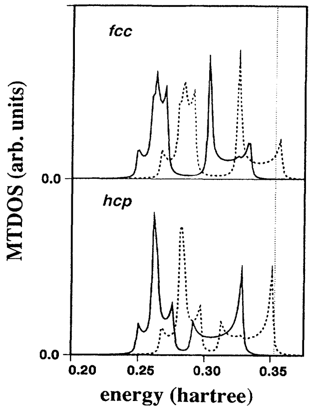

FIG. 7. A comparison of the Γ-projected MTDOS for bulk fcc nickel (upper panel) and bulk hcp nickel (lower panel). The solid lines are the majority-spin states and the dashed lines are the minority-spin states. The vertical dotted line represents the Fermi level of fcc nickel (the position of the Fermi level of hcp nickel is indistinguishable at this scale). The width of the $d$ band nearest to the Fermi level is noticeably increased in the hcp structure. This broadening can be correlated with a reduction in spin polarization, which is consistent with the simple Stoner theory of magnetism which suggests that spin polarization is inversely related to the bandwidth.

density of atoms along the [0001] direction of the hcp structure, which is the direction equivalent to the {111} directions of fcc structure, is higher than that found in the fcc structure. The calculated reduced spin polarization in the hcp structure is consistent with the simple Stoner theory of magnetism which suggests that spin polarization is inversely proportional to the bandwidth. Figure 8 is the MTDOS of hcp and fcc nickel plotted at $\overline{M}$. The $\overline{M}$ point includes the states which lie along the line connecting $X$ and $L$ of the fcc three-dimensional Brillouin zone (the corresponding direction in the hcp zone is the $L$ to $M$ direction). The most significant feature of this plot is the peak in the majority-spin density of states which appears *above* the Fermi level in the hcp structure. In addition, a gap opens in the majority-spin states at the Fermi level. In the fcc structure, the majority-spin states which cross the Fermi level lie near the $L$ point and the majority-spin $d$ states nearest to the Fermi level lie at the $X$ point. In going to the hcp structure, the cubic symmetry is lost and the states at $L$ and $X$ are mixed, resulting in the observed changes, including the gap at the Fermi level and the majority-spin peak above it. The result of this symmetry-driven change is that majority-spin states, mostly $p$ states, are pushed above the Fermi level and the electrons formerly in those states are forced to occupy the minority-spin $d$ states along the Γ to $A$ direction of the hcp zone.

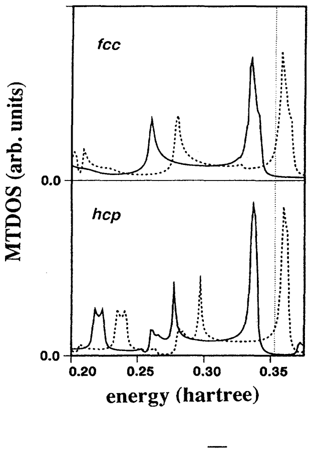

FIG. 8. A comparison of the $\overline{M}$-projected MTDOS for bulk fcc nickel (upper panel) and bulk hcp nickel (lower panel). The solid lines are the majority-spin states and the dashed lines are the minority-spin states. There is a symmetry-induced rearrangement of the majority-spin states near the Fermi level in going from the fcc to the hcp structure; a gap opens in the majority states and a peak appears above the Fermi level. The rearrangement of states pushes majority-spin states of mostly $p$ character above the Fermi level. The electrons which formerly occupied these states are then forced to occupy minority-spin states near the Fermi level.

The physics underlying the differences between hcp nickel and fcc nickel can also help to explain the small changes in spin polarization observed near a stacking fault. There are two types of layers which appear in the stacking sequences. One type, which has the local symmetry (i.e., all 12 nearest neighbors and their relative locations) of the hcp lattice, trigonal prismatic, is referred to as a $P$ layer. The other layers, which have the local structure of the fcc lattice, octahedral, are referred to as $O$ layers. The hcp lattice is composed entirely of $P$ layers and the fcc lattice is composed entirely of $O$ layers. The stacking-fault structures studied here are composed of $P$ layers embedded in an $O$ layer bulk. These $P$ layers might be expected to have some of the properties of the hcp bulk.

Consider the twin-boundary fault, which consists of one isolated $P$ layer in an otherwise fcc structure. The most unusual feature of this fault is that the layers with the spin polarization of the bulk hcp lattice are actually the $O$ layers immediately adjacent to the $P$ layer. Furthermore, the $P$ layer of the fault has a spin polarization near that of the fcc structure. This trend is exactly opposite to what one would expect from naive arguments based on local structure, but can, in fact, be understood quite simply as follows. In the twin-boundary fault, the $O$ layers immediately adjacent to the $P$ layer each have one neighbor in the [111] direction at a distance of two (111) planes away, whereas in the fcc structure each atom has two neighbors at a distance of three (111) planes away. The presence of a neighbor at only two (111) atomic planes away results in a local broadening of the MTDOS associated with the states with wave vectors along the Γ to $L$ direction, which are exactly the states that appear broadened when going from the fcc structure to the hcp structure. This local broadening is apparent in the $\overline{\Gamma}$ layer-projected MTDOS for the twin-boundary fault (Fig. 5).

This local broadening of the $\overline{\Gamma}$ MTDOS on layers with neighbors in the [111] direction at a distance of only two (111) planes away is a feature common to all of the studied faults, and the spin polarization of these layers is reduced relative to the bulk fcc value. (This reduction, while very small, is believed to be a real prediction of local-density-functional theory, and does not arise from the slight charge imbalance of the stacking faults which could account for at most $0.001\mu_B$ of the change in moment.) It is worthwhile noting that the largest calculated reduction in spin polarization appears on the central *O* layer of the extrinsic fault—a layer with two neighbors along the [111] direction at a distance of two (111) planes away. [Examination of the $\overline{M}$ spectral function (not shown) of the extrinsic fault reveals the beginnings of the formation of the majority-spin peak above the Fermi level as well.] The relationship between spin polarization and neighbors in the [111] direction can be made more quantitative, and is discussed in Sec. V.

The small changes in spin polarization would most likely not be present if the Fermi level did not cross those bands composed of states with **k** along the [111] direction. Thus the mechanism of the reduction in spin polarization seems very specific to nickel. This, however, may not be the case. The band structure of cobalt[26] shows some of the very features necessary to produce the observed effects: A minority-spin *d* band crosses the Fermi level along the $\Gamma$ to *A* direction (equivalent to the [111] direction in the fcc structure), and the majority-spin band along the *M* to *L* direction of the hcp zone nearest to the Fermi level is in nearly the same configuration relative to the Fermi level as that in hcp nickel. The presence of *O* layers in the *P* layer bulk of cobalt may, therefore, result in an enhanced spin polarization on the *O* layers.

### B. Electronic structure

Figures 5 and 6 are the layer-projected MTDOS for the twin-boundary fault plotted at $\overline{\Gamma}$ and $\overline{K}$, respectively. The most notable feature of Fig. 5 is the pronounced resonant state which splits off the lower edge of the upper *d* bands for both spin polarizations. This resonance is present in all the studied faults, and effectively increases the local bandwidth. Three localized states are apparent in the $\overline{K}$ MTDOS (Fig. 6), one at 0.307 hartree (0.330 hartree), another at 0.289 hartree (0.308 hartree), and a third state at 0.205 hartree (0.221 hartree) in the majority (minority) -spin MTDOS.

The twin-boundary fault is unique among the faults studied in that it is the only fault with one *P* layer. The remaining faults each contain two *P* layers with a various number of intervening *O* layers, ranging from zero in the intrinsic fault to 3 in the hyperextrinsic fault. It is interesting to study to what extent *P* layers interact when separated by different numbers of planes.

A simple anlaysis suggests the following arguments. Consider the $\overline{K}$ point of the two-dimensional Brillouin zone. Each *P* layer should result in three states localized at that *P* layer. Therefore, in the faults with two *P* layers, there should be six states localized at the faults. Interactions between the states centered on different *P* layers should split the states, resulting in three symmetric and three antisymmetric states. Inspection of Table III, however, reveals that, at most, four localized states appear at the faults.

Figure 9 is the layer-projected MTDOS for $\overline{K}$ of the hyperextrinsic fault. The localized state at 0.205 hartree (0.222 hartree) in the majority (minority) spin appears to be the antisymmetric state of a symmetric-antisymmetric pair (i.e., the state has a node on the central layer of the fault). However, it may be simply that the state is very well localized and does not interact with the localized state centered on the other *P* layer of the fault. Inspection of the $\overline{K}$ MTDOS for the twin-boundary fault (Fig. 6) suggests that this is in fact the case. The localized state at 0.205 hartree has zero spectral weight on all but the *P* layer and the two *O* layers immediately adjacent to it. The same holds true for the state at 0.289 hartree (0.308 hartree) in the majority (minority) spin. The states at 0.308 and 0.306 hartree in the majority-spin band do, however, appear to be a symmetric-antisymmetric pair. (The state at 0.308 hartree is the antisymmetric state.) So simple arguments explain the behavior of the hyperextrinsic fault quite well.

It is not a bold step to assume that as the *P* layers are brought closer together, the interactions between the states localized on different *P* layers will become larger. If this were the case, one would expect the splitting ob-

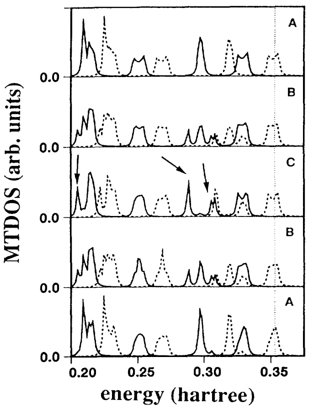

FIG. 9. The layer-projected MTDOS for the $\overline{K}$ point of the hyperextrinsic fault. The solid curves are the majority-spin states and the dashed curves are the minority-spin states. The dotted line represents the Fermi energy. The arrows indicate the majority-spin localized states. (The corresponding minority-spin localized states, *not* indicated by arrows, lie approximately 0.02 hartree above their majority-spin counterparts.) (The energies and exchange splittings of the states are given in Table III.) The states at 0.308 and 0.306 hartree in the majority-spin states, indicated by only one arrow, appear to be a symmetric-antisymmetric pair of states split by interactions between the states centered on different *P* layers. This splitting, which is present even in non-self-consistent calculations, is not observed in any of the other faults and appears to be related to the specific structure of the hyperextrinsic fault and the states involved in the splitting.

served in the hyperextrinsic fault to be smaller than that in the superextrinsic fault. Surprisingly, no splitting is observed in the superextrinsic or even in the extrinsic fault. The states on different *P* layers appear to be essentially noninteracting, until the *P* layers are immediately adjacent (the intrinsic fault). It is not easy to understand these observations within a simple theory. The splitting observed in the hyperextrinsic fault appears to be a symmetry-induced phenomena (it is present even in non-self-consistent calculations) which depends on the detailed structure of the hyperextrinsic fault, as well as on the nature of the localized states.

## V. SIMPLE EMPIRICAL EXPRESSIONS

As discussed in Sec. IV, the spin polarization of a layer is most sensitive to the distribution of atoms along the [111] direction orthogonal to the fault plane, and is not very sensitive to the orientations of the nearest and next-nearest neighbors. This dependence can be described quantitatively.[21] The spin polarization of any layer can be fitted to an expression of the form

$$\mu = M_0 + \sum_{i=2}^{3} \eta_i \alpha_i \ , \tag{3}$$

where $\mu$ is the spin polarization of the layer under consideration and $\mu_i$ is the number of layers, *i* layers away, that are identical to the layer under consideration, (e.g., for the fcc structure, $\eta_2=0$ and $\eta_3=2$, while for the hcp case, $\eta_2=2$ and $\eta_3=0$). From structural considerations, $\eta_1=0$ always. The parameters $M_0$, $\alpha_2$, and $\alpha_3$ are fitted to the results of all calculations based on the bulk fcc structures (i.e., *not* including the bulk hcp results). The fits were performed giving the fcc bulk result an infinite weight resulting in a two-parameter fit. (The parameters $M_0$ and $\alpha_3$ are *not* independent because of the infinite weight given to the bulk fcc result.) The fitting parameters have the values $M_0=0.584\mu_B$ and $\alpha_2=-0.005\mu_B$. The results of the fitting for the extrinsic and intrinsic faults are shown in Fig. 10. The fit accurately reproduces the trends in spin polarization for all of the faults. The predicted value of the hcp bulk spin polarization is $0.573\mu_B$, a result slightly smaller than that calculated by the LKKR method. This discrepancy probably stems from the fact that the Fermi level in the hcp bulk differs from that of the fcc bulk, and the simple linear fitting scheme described above cannot be expected to be fully reliable.

The energy of the stacking faults can also be modeled by a simple linear fitting scheme. The energy of the stacking faults is fitted to the following expression:

$$E = \sum_{\text{layers}} \left[ E_p + \sum_{i=2}^{4} \xi_i \gamma_i \right] , \tag{4}$$

where $E_p$ is zero for *O* layers and a nonzero constant for *P* layers and $\xi_i$ is the number of planes located *i* (111) layers away that are different from what they would be in the fcc case (e.g., $\xi_2=2$, $\xi_3=2$, and $\xi_4=2$ for the hcp lattice). The parameters $E_p$ and the $\gamma_i$'s are energies to be fitted to the complete calculation. They are given in Table V. The resulting energies, as given by (4), are contained in Table II. Overall, the fitted energies are in reasonable agreement with the energies calculated by the LKKR method and are certainly in reasonable agreement with the experimental values.

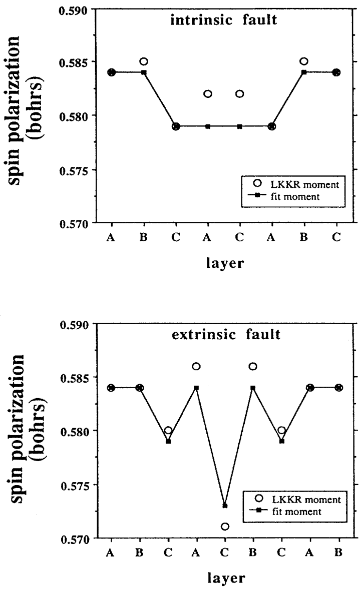

FIG. 10. A comparison of the LKKR spin polarization and spin polarizations predicted by the simple fitting scheme for the intrinsic and extrinsic faults. The solid lines are guides for the eye. The simple formula accurately reproduces the trends in spin polarization for both pictured faults. Fits to the LKKR data for other faults are equally good.

Hirth and Lothe[27] suggested, based upon geometrical arguments, an expression for the energy of the twin-boundary, intrinsic, and extrinsic stacking faults in fcc metals. The resulting formulas were expressed in terms of pairwise bonding interactions. Including the effects from up to the eighth nearest neighbor suggests that

$$E_{\text{int}} = E_{\text{ext}} = 2E_{\text{twin}} \ . \tag{5}$$

The results presented here give roughly the same relationship between energies, but show a slight reduction in energy for the intrinsic and extrinsic faults, possibly arising from interactions between adjacent *P* layers. The energies calculated here are not precise enough to draw strong conclusions. The *P* layers do interact, however, as is aptly demonstrated by the splitting of the states in the hyperextrinsic fault, and the energy of the extrinsic fault does seem to be slightly less than twice the twin-boundary fault energy.

TABLE V. Energy fitting parameters (erg/cm$^2$).

| | |
|---|---|
| $E_p$ | 67 |
| $\gamma_2$ | 13 |
| $\gamma_3$ | $-10$ |
| $\gamma_4$ | 3 |

The fitted fault energies and the splitting of the localized electronic states suggest anomalous behavior for the hyperextrinsic fault. Its energy is predicted to be twice the twin-boundary-fault energy, but the faults with four and five layers separating the $P$ layers are predicted to have lower energies (156 erg/cm$^2$), thus making the hyperextrinsic fault a local maximum in the energy versus separation curve.

## VI. CONCLUSIONS

The electronic and magnetic properties of {111} stacking faults in nickel have been calculated using a fully self-consistent LKKR formalism which does not require finite-sized slabs or periodic boundary conditions. The total energies and spin polarizations of all of the faults were calculated and tabulated. The total energies were found to be in good agreement with experiment.

The reported changes in spin polarization are very small (less than 2%). Nevertheless, the mechanism behind the reduction appears to be a physical prediction of the local-density-functional theory used to calculate the properties. The decrease in spin polarization can be related to the distance to the nearest neighbor in the [111] direction, and does not seem to depend on the changes in the relative orientations of the nearest neighbors. The close proximity of atoms in the [111] direction results in a local broadening of the states formed from the band states with **k** along the [111] direction. This broadening is accompanied by a symmetry-induced rearrangement of the majority-spin states near the Fermi level, and results in a slight decrease in spin polarization. These effects, while depending directly on the specific features of the nickel band structure, may be present in cobalt stracking faults.

Localized states appear at all of the studied faults. Their energies are calculated and tabulated. The splittings of the states suggest anomalous behavior for the hyperextrinsic fault, i.e., that fault in which two trigonal prismatic layers are separated by three (111) close-packed planes. These localized states may be observable in photoemission experiments, but the presence of surface states may mask the stacking-fault states.

Finally, simple empirical fits are used to describe both the spin polarization and total energy of any stacking sequence. The fits are in reasonable agreement with both the experimental and LKKR results. The formulas should be useful for analyzing more complicated stacking sequences.

## ACKNOWLEDGMENTS

The authors gratefully acknowledge D. D. Johnson and Rob Phillips for lively discussions and a careful reading of this manuscript. Insightful discussions with M. J. Mills are also gratefully acknowledged. The work performed at Sandia National Laboratories was supported by the U.S. Department of Energy, Office of Basic Energy Sciences, Division of Materials Science. The work at Lawrence Berkeley Laboratory was supported by the U.S. Department of Energy, Office of Basic Energy Sciences under Contract No. DE-AC03-76SF00098. The work performed at Lawrence Livermore National Laboratory was supported by the U.S. Department of Energy, Contract No. W-7405-ENG-48. Some of the computational work was performed under a grant from the U.S. Department of Energy. The authors also acknowledge partial support from the Office of Naval Research.

---

[1] S. Blügel, M. Weinert, and P. H. Dederichs, Phys. Rev. Lett. **60**, 1077 (1988).

[2] C. L. Fu, A. J. Freeman, and T. Oguchi, Phys. Rev. Lett. **54**, 2700 (1985).

[3] R. Richter, J. G. Gay, and J. R. Smith, Phys. Rev. Lett. **54**, 2704 (1985).

[4] J. Tersoff and L. M. Falicov, Phys. Rev. B **26**, 6186 (1982).

[5] R. H. Victora and L. M. Falicov, Phys. Rev. B **31**, 7335 (1985).

[6] L. M. Falicov, R. H. Victora, and J. Tersoff, in *The Structure of Surfaces,* edited by M. A. Van Hove and S. Y. Tong (Springer-Verlag, Heidelberg, 1985), p. 12.

[7] M. Stamponi, A. Vaterlaus, D. Pescia, M. Aeschlimann, F. Meier, W. Dürr, and S. Blügel, Phys. Rev. B **37**, 10 380 (1988).

[8] W. Drube and F. J. Himpsel, Phys. Rev. B **35**, 4131 (1987).

[9] D. E. Eastman, F. J. Himpsel, and J. A. Knapp, Phys. Rev. Lett. **40**, 1514 (1978).

[10] *Magnetic Properties of Low-Dimensional Systems,* edited by L. M. Falicov and J. Morán-López, (Springer-Verlag, Heidelberg, 1986).

[11] D. L. Abraham and H. Hopster, Phys. Rev. Lett. **62**, 1157 (1989).

[12] W. Dürr, M. Taborelli, O. Paul, R. Germar, W. Gudat, D. Pescia, and M. Landolt, Phys. Rev. Lett. **62**, 206 (1989).

[13] D. Mauri, D. Scholl, H. C. Siegmann, and E. Kay, Phys. Rev. Lett. **62**, 1900 (1989).

[14] L. E. Klebanoff, R. H. Victora, L. M. Falicov, and D. A. Shirley, Phys. Rev. B **32**, 1997 (1985).

[15] F. Yndurain and L. M. Falicov, Phys. Rev. Lett. **37**, 928 (1976).

[16] W. R. Grise, L. Kleinman, and K. Mednick, Phys. Rev. B **22**, 1729 (1980).

[17] J. M. MacLaren, S. Crampin, D. D. Vvedensky, and J. B. Pendry, Phys. Rev. B **40**, 12 164 (1989).

[18] J. B. Pendry, *Low Energy Electron Diffraction* (Academic, London, 1974).

[19] L. Hedin and B. I. Lundqvist, J. Phys. C **4**, 2064 (1971).

[20] D. D. Koelling and B. N. Harmon, J. Phys. C **10**, 3107 (1977).

[21] D. C. Chrzan, L. M. Falicov, J. M. MacLaren, X.-G. Zhang, and A. Gonis, J. Appl. Phys. **67**, 4558 (1990).

[22] V. L. Moruzzi, J. F. Janak, and A. R. Williams, *Calculated Electronic Properties of Metals* (Pergammon, New York, 1978).

[23] C. S. Wang and J. Callaway, Phys. Rev. B **15**, 298 (1977).

[24] C. Barret and T. B. Massalski, *Structure of Metals,* 3rd ed. (McGraw-Hill, New York, 1965), pp. 387–390, 440–453.

[25] C. B. Carter and S. M. Holmes, Philos Mag. **35**, 1161 (1977).

[26] D. A. Papaconstantopoulos, *Handbook of the Band Structure of Elemental Solids* (Plenum, New York, 1986).

[27] J. P. Hirth and J. Lothe, *Theory of Dislocations* (Wiley, New York, 1982); L. E. Murr, *Interfacial Phenomena in Metals and Alloys* (Addison-Wesley, Reading, MA, 1975).

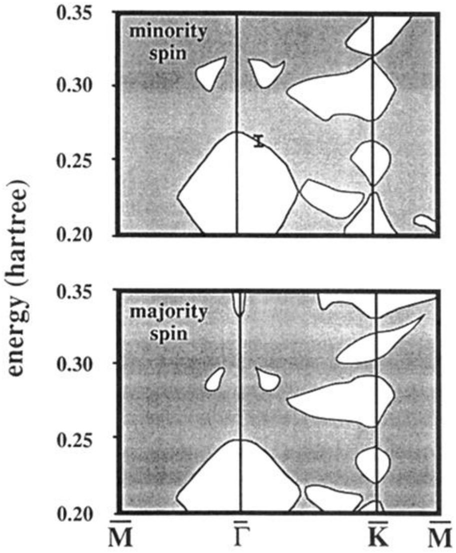

FIG. 4. The two-dimensional projected band structure of bulk fcc nickel. The shaded regions of this plot correspond to points for which three dimensionally extended band states exist. The white regions, in which no three-dimensional band states are found, are the regions where localized states may be found. The error bar indicates the accuracy to which the figure is drawn. From the figure it is clear that localized states (in the depicted energy range) may be found near $\overline{\Gamma}$ and $\overline{K}$, but not near $\overline{M}$.